

PRIMA: Boosting Animal Mesh Recovery with Biological Priors and Test-Time Adaptation

Xiaohang Yu, Ti Wang, and Mackenzie Weygandt Mathis

École Polytechnique Fédérale de Lausanne (EPFL)
mackenzie.mathis@epfl.ch

Abstract. We present PRIMA (**PRI**ors for **M**esh **A**daptation), a framework for robust 3D quadruped mesh recovery under severe species and pose imbalance. Existing animal reconstruction methods often regress toward mean shapes and poses due to limited 3D supervision and long-tailed species distributions, resulting in poor generalization to underrepresented animals and rare articulations. PRIMA addresses this challenge through three key contributions. First, we incorporate BioCLIP embeddings as biological priors to inject semantic and morphological knowledge into the reconstruction process, enabling more accurate and generalizable shape prediction across diverse quadrupeds. Second, we introduce a test-time adaptation (TTA) strategy that refines SMAL predictions using 2D reprojection constraints together with auxiliary keypoint guidance, improving pose and shape estimation while enabling the generation of high-quality pseudo-3D annotations from existing 2D datasets. Third, leveraging this TTA framework, we construct Quadruped3D, a large-scale pseudo-3D dataset that covers diverse species and pose variations to systematically improve model performance. Extensive experiments on Animal3D, CtrlAni3D, Quadruped2D, and Animal Kingdom demonstrate that PRIMA achieves state-of-the-art results, with particularly strong improvements on underrepresented species and challenging poses. Our results highlight the importance of biological priors and adaptation-driven data expansion for scalable and generalizable animal mesh recovery. Code is available at <https://github.com/AdaptiveMotorControlLab/PRIMA>.

Keywords: animal mesh recovery · biological priors · test-time adaptation · 3D animals

1 Introduction

Reconstructing the 3D shape and pose of animals from monocular imagery is a fundamental task with far-reaching implications for ecology, neuroscience, and biodiversity monitoring. However, reconstructing the 3D geometry and pose from a single image is an ill-posed problem that shares similar challenges as general 3D reconstruction [8, 35, 45, 51], such as depth ambiguity and occlusion, while raising additional challenges that are specific to animals, including large inter-class and intra-class shape variation, diverse articulation patterns, and the scarcity of high-quality 3D supervision [24]. Similar to human mesh recovery,

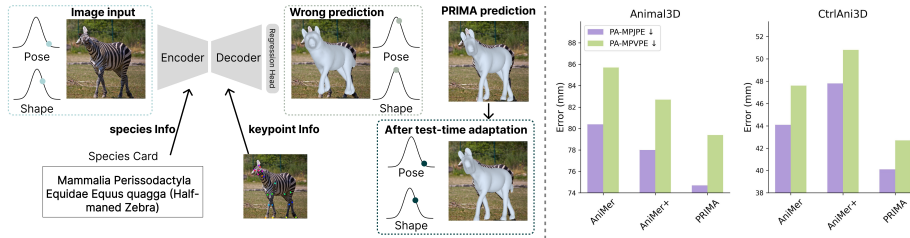


Fig. 1: Overview of PRIMA. Due to the unbalanced distribution of 3D animal training data, vanilla networks often suffer from mean regression bias, yielding implausible meshes that collapse toward the average shape of majority species (e.g., a “dog-like” zebra in wrong prediction). We propose to inject biological taxonomies and keypoint-aware tokens as strong inductive biases into the latent space. This semantic anchoring effectively constrains the search space, shifting the model from a biased global prior to a precise conditional posterior (PRIMA prediction). Notably, even before test-time adaptation, PRIMA significantly outperforms baselines in alignment and joint accuracy (right). Our Test-Time Adaptation loop further refines these parameters for instance-specific precision.

the use of strong shape and pose priors has proven essential to constrain the solution space [10, 26, 34]. To this end, SMAL [57] introduced a 3D articulated model for quadruped animals, parameterizing animal shape and pose through a low-dimensional representation learned from aligned 3D animal scans. This pioneering work provides a unified and differentiable parametric representation of animal geometry, allowing optimization-based and learning-based monocular 3D reconstruction in a manner analogous to SMPL [26] for humans.

Despite this progress, accurately modeling animals in the wild remains a challenge. A primary difficulty lies in the extreme inter-class and intra-class morphological variability of animals. Unlike humans, whose skeletal topology is largely consistent, animals exhibit substantial structural diversity across families. Inter-class variation manifests in pronounced differences in body proportions and limb configurations, such as the contrast between felids and ungulates, while intra-class variation is also significant, particularly in breed-level differences observed in species like dogs. To cope with such diversity, several works focus on species-specific architectures and curated datasets, targeting dogs [4, 5, 7, 21, 38–40, 42], horses [22, 23, 58], zebras [56], and birds [2, 18, 44]. While effective within restricted domains, these approaches lack scalability and leave many species underrepresented, such as cats and hippopotamuses. To address this, 3D Fauna [25] introduces a pan-category semantic space, learning a unified model for diverse quadrupeds from large collections of 2D images. However, although 3D-Fauna provides a strong zero-shot baseline via structural inductive biases, it often lacks instance-specific fidelity for complex articulated poses due to missing dense 3D supervision. More recent efforts [1, 28] attempt to model multiple species within a unified framework using family-aware transformers. However, existing 2D and

3D datasets exhibit highly imbalanced family-level distributions, where families such as Canidae and Equidae dominate the training data, while others like Felidae, Bovidae, and Hippopotamidae are significantly under-represented. Under such long-tailed distributions, models trained in a purely data-driven manner tend to bias predictions toward majority families. As a result, implicitly inferring the animal family from appearance alone often leads to biased shape estimation and a collapse toward average shapes of over-represented categories.

The second challenge involves high-dimensional pose variation and the lack of ground-truth (GT) observations. Animals are highly dynamic, showcasing a vast range of non-rigid motions and extreme deformations that lead to frequent self-occlusions and complex silhouettes. While human reconstruction tasks benefit from large-scale, high-fidelity Motion Capture datasets [9, 15, 30, 36, 53] and large fitting [11] datasets for pGT, obtaining 3D ground truth for animals in the wild remains highly challenging. Several studies [5, 46] employ optimization-based fitting pipelines, often supplemented with manual inspection, to obtain pseudo-SMAL annotations. However, these optimization frameworks are typically computationally intensive and demand considerable human effort, which substantially limits their scalability. Other works [19, 28, 31, 33, 55, 56] instead focus on synthetic animal datasets, leveraging generative models to produce artificial animal instances. However, there still exists a domain gap between synthetic data and real-world data. To this end, we incorporate a test-time adaptation protocol based on our pre-trained framework by leveraging keypoint-aware tokenization to refine SMAL predictions through 2D reprojection constraints, thereby distilling high-fidelity pseudo-3D annotations from 2D datasets.

To address these challenges, we introduce PRIMA, a framework for accurate 3D animal pose and shape estimation from a monocular image (Fig. 1). Our approach combines biological priors, test-time adaptation, and large-scale pseudo-3D data to improve reconstruction accuracy, generalization, and robustness across diverse quadrupeds. Our contributions are three-fold:

Biological priors for generalizable mesh recovery. We leverage Bio-CLIP [41] embeddings to inject semantic and morphological knowledge into the reconstruction process. By grounding the model in biologically plausible priors, PRIMA achieves more accurate shape predictions for underrepresented animals, outperforming prior methods that tend to bias toward majority species while still generalizing across diverse quadrupeds.

Test-time adaptation for high-fidelity per-instance refinement. We introduce a test-time adaptation (TTA) protocol that refines SMAL predictions using 2D reprojection consistency, enabling precise per-instance shape and pose estimates. This procedure substantially improves pose and shape accuracy, particularly for complex or challenging poses.

Quadruped3D dataset for model enhancement. Leveraging our TTA framework, we automatically construct Quadruped3D, a large-scale pseudo-3D dataset encompassing a wide range of quadruped species and pose variations. This dataset enables systematic improvement of model performance, enhances

the fidelity of pose estimation, and serves as a valuable benchmark and resource for subsequent research in the reconstruction of animal morphology and motion.

2 Related Work

2.1 Learning-based Animal Mesh Recovery

The primary challenge in learning-based 3D animal reconstruction lies in the extreme morphological diversity across species and the inherent scarcity of 3D ground truth. Early research addressed this by developing high-fidelity regressors for well-documented species, such as BARC [38], BITE [39], DogRecon [7], and Animal Avatars [40] for dogs, or specialized frameworks for horses [58], zebras [56], and birds [18, 44]. While these methods achieve impressive results within their respective domains, their reliance on category-specific priors limits their scalability to the vast "long-tail" of animal species found in the wild.

To overcome this bottleneck, recent works have shifted toward unified frameworks. Some works [20, 25, 48, 49] learn pan-category models from image or video collections via a shared shape bank or canonical surface mapping, while AniMer [28] utilizes family-aware transformers to handle diverse quadrupeds. AniMer+ [1] further extends this scope to birds by incorporating a Mixture-of-Experts (MoE) design to manage inter-class variance. However, existing methods remain constrained by the long-tail distribution of animal datasets, where a few dominant species bias the model, limiting generalization to sparsely observed taxa. To mitigate this, our work incorporates a biological structural prior derived from BioCLIP [41], a pre-trained taxonomic foundation model. By leveraging its hierarchically structured species embeddings, we provide a unified geometric constraint that improves robustness across the long tail without requiring explicit per-species supervision.

2.2 Analysis-by-Synthesis and Test-Time Adaptation

The "Analysis-by-Synthesis" paradigm aims to resolve the inherent ambiguity of single-view reconstruction by minimizing the discrepancy between 2D observations and 3D projections. Traditional fitting-based methods directly optimize the pose and shape parameters of parametric models, as seen in SMPLify [6] and SMPLify-X [34] for humans [26], and SMALify [5] for animals. Although these methods provide high-precision alignment using sophisticated priors such as HuMoR [37] or KBody [54], they are computationally intensive and highly sensitive to initializations.

To combine feed-forward efficiency with optimization precision, recent 3D human works adopt post-optimization, using a pre-trained network for robust initialization followed by iterative refinement, as in ISO [52], EFT [16], DynaBOA [14], and CycleAdapt [32]. More advanced methods, such as ESCAPE [3] and UAO [43], add uncertainty-aware or cyclic constraints for stable refinement.

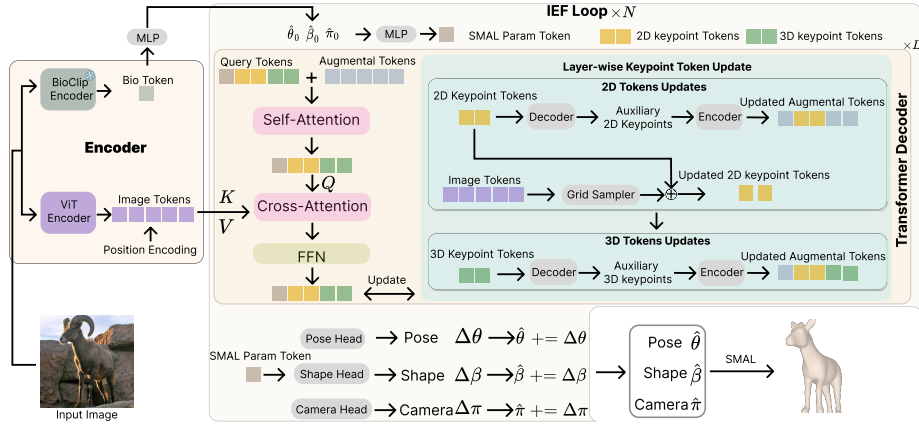


Fig. 2: **Overview of the proposed model architecture.** Given an input image, a ViT encoder extracts image tokens and a BioCLIP encoder produces a bio token. An MLP maps the bio token to initialize the SMAL shape parameter $\hat{\beta}_0$, and the SMAL parameters are projected into a SMAL parameter token. The transformer decoder and regression heads follow an Iterative Error Feedback (IEF) scheme for N iterations. Across L layers, query tokens augmented with zero-initialized augmental tokens undergo self-attention, cross-attention to image tokens, and an FFN, followed by a layer-wise keypoint token update module that refines augmental tokens and 2D keypoint tokens. Finally, pose, shape, and camera heads regress $(\Delta\theta, \Delta\beta, \Delta\pi)$ from the SMAL parameter token to update the parameters and obtain the final mesh.

3DB [47] further treats multi-view optimization as post-processing on single-view predictions. However, directly extending these strategies to animal mesh recovery is challenging due to large morphological variation.

Our TTA-driven self-distillation pipeline innovates by constraining the optimization specifically to the keypoint tokens and decoder heads. This localized update ensures that the instance-specific refinement remains grounded in the pre-trained backbone’s structural prior. Crucially, unlike existing refinement strategies that serve only as post-processing, we utilize TTA as a data evolution engine. By distilling high-confidence pseudo-labels, we curate the Quadruped3D dataset, expanding our supervision from 13K to a unified 23K training pool. This iterative loop allows the feed-forward network to internalize the precision of optimization across the animal kingdom.

3 Methods

3.1 Preliminaries

SMAL [57] is a parametric model that represents 3D mesh geometry with shape parameters $\beta \in \mathbb{R}^{41}$ and pose parameters $\theta \in \mathbb{R}^{105}$, enabling diverse

quadruped shapes and articulated poses. Given these parameters, SMAL defines a differentiable function that outputs a 3D mesh $m \in \mathbb{R}^{3889 \times 3}$. To fit the SMAL model to a given animal image or video, SMALify [5] adopts an optimization-based fitting procedure that estimates the SMAL parameters by minimizing reprojection errors with respect to 2D keypoints and silhouette observations.

BioCLIP [13, 41] is a vision foundation model for the tree of life, trained on large-scale biological data spanning diverse organisms (including a wide range of animal species) with hierarchical taxonomic labels. The image encoder maps an input image to a species-aware embedding in a shared feature space, capturing morphology-related cues and species-level semantic information.

3.2 Model Architecture

As shown in Figs. 1 and 2, our model adopts an encoder-decoder design with two parallel visual encoders. A ViT extracts image tokens, while a BioCLIP encoder produces a bio token for bio-guided shape parameter initialization. A keypoint-aware transformer decoder refines learnable keypoint and parameter tokens layer by layer, and regression heads predict residual updates to the SMAL parameters to recover the final 3D animal mesh.

Image Encoders. To capture both general appearance and species semantics, we extract features from two parallel encoders applied to the cropped and normalized animal image I . A standard ViT encoder f_{ViT} produces general image features:

$$F_{\text{img}} = f_{\text{ViT}}(I) \in \mathbb{R}^{N \times D}, \quad (1)$$

where N denotes the number of visual tokens and D denotes the feature dimension. And a frozen BioCLIP encoder f_{bio} produces species-aware features:

$$F_{\text{bio}} = f_{\text{bio}}(I) \in \mathbb{R}^{1 \times 768}. \quad (2)$$

The image feature F_{img} captures instance-specific visual details, whereas F_{bio} encodes biological priors that reflect taxonomic semantics. To leverage biological knowledge and alleviate the challenges posed by the unbalanced category distributions, we introduce a bio-informed coarse-to-fine shape initialization strategy. Instead of initializing SMAL shape parameters from a zero vector or a generic mean template, we first derive a taxonomic shape prior from the species-aware features, which provides a semantically meaningful initialization in the SMAL shape space. Subsequent geometric refinement is then performed by the transformer decoder, conditioned on image features.

Concretely, the species-aware features are projected into a shared latent space to form a bio-token T_{bio} . The initial SMAL shape parameter is predicted as:

$$\beta_{\text{init}} = \mathcal{M}(T_{\text{bio}}) \in \mathbb{R}^{1 \times 41}, \quad (3)$$

where \mathcal{M} is a multi-layer perceptron (MLP) that maps the semantic biological prior to the SMAL shape parameter space.

Keypoint-aware Decoder. Inspired by the keypoint tokens in 3DB [47] for human pose decoding, we propose a Keypoint-Aware SMAL Decoder, a transformer-based iterative refinement module that integrates structured token reasoning for animal mesh recovery. Unlike previous methods [28] that directly regress pose and shape parameters from global features via regression heads, our decoder explicitly models SMAL parameter token and keypoint tokens, enabling structured reasoning through self-attention and cross-attention to image features.

To facilitate progressive geometric reasoning, we leverage a layer-wise keypoint re-grounding mechanism within the transformer decoder. Specifically, after each decoder layer (except the last), the 2D and 3D keypoint tokens are explicitly decoded into coordinate predictions. The predicted 2D coordinates are used to sample image-aligned features from the visual feature map via differentiable grid sampling, while the 3D coordinates are refined in latent space. The sampled or refined features are then fused back into the corresponding keypoint tokens, forming dynamically grounded token representations for the subsequent layer. This design enables intermediate geometric alignment and progressively refines keypoint hypotheses across layers.

The complete set of query tokens is defined as:

$$T = [T_{\text{param}}, T_{2\text{Dkeypoint}}, T_{3\text{Dkeypoint}}], \quad (4)$$

where T_{param} , $T_{2\text{Dkeypoint}}$, and $T_{3\text{Dkeypoint}}$ denote the SMAL parameter, 2D keypoint, and 3D keypoint query tokens, respectively. The transformer decoder \mathcal{D} first performs self-attention over the query tokens T , followed by cross-attention with the image features F_{img} , producing:

$$O = \mathcal{D}(T, F_{\text{img}}) \in \mathbb{R}^{(1+2J) \times D}, \quad (5)$$

where \mathcal{D} consists of stacked self-attention, cross-attention, and feed-forward layers, and J denotes the number of joints. Through cross-attention, the decoder integrates keypoint-aware representations with visual context, enabling structured shape and pose estimation.

The first output token of O is fed into regression heads to predict residual mesh parameters, namely pose, shape, and camera. The remaining tokens are decoded as auxiliary 2D and 3D keypoint predictions.

3.3 Model training

Training Loss. Our model is trained with a multi-task loss term:

$$\mathcal{L} = \lambda_{\text{param}} \mathcal{L}_{\text{param}} + \lambda_{\text{keypoint}} \mathcal{L}_{\text{keypoint}}. \quad (6)$$

Parameter Losses. For 3D data with SMAL parameters, we directly supervise them with L_2 regression losses and also prior losses are imposed to encourage plausible poses.

2D/3D Keypoint Loss. Keypoint losses consist of two folds. First is the auxiliary 2D and 3D keypoint output from the SMAL decoder as deep supervision to enable 2D and 3D keypoint reasoning. And the second is the 2D and 3D

keypoint regressed from the mesh to ensure reprojection correctness. Both folds are supervised with L_1 loss.

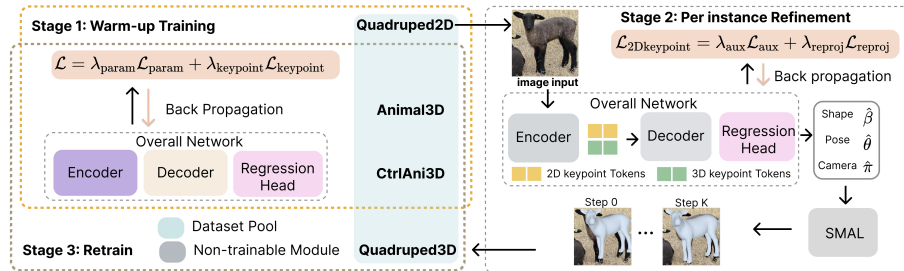


Fig. 3: **Overview of the proposed three-stage training framework.** The proposed methodology consists of an alternating three-stage training paradigm. Stage 1, warm-up training, leverages available 3D datasets and a 2D dataset to initialize the model parameters. Stage 2, per-instance refinement, then optimizes pose and shape parameters under 2D keypoint supervision to construct pseudo Ground Truth (pGT) SMAL parameters for the Quadruped2D dataset. Finally, Stage 3, loop-back retraining, performs a subsequent retraining phase that incorporates the refined instances together with the original 3D datasets, thereby further enhancing model performance.

3.4 Test-time Adaptation

Although trained on large-scale data, feed-forward predictors inevitably suffer from domain shift and articulation ambiguity in unconstrained in-the-wild settings. To systematically mitigate this gap, we introduce a principled test-time adaptation (TTA) scheme that performs controlled instance-level refinement of SMAL parameters using only 2D keypoint supervision.

As shown in Stage-2 in Fig. 3, starting from the Stage-1 pre-trained model, we freeze the encoder and decoder, and optimize only the SMAL regression head and the 2D/3D keypoint tokens. This design preserves the learned geometric prior, while retaining sufficient flexibility for instance-level pose and shape refinement. The optimization objective is defined as:

$$\mathcal{L}_{2\text{Dkeypoint}} = \lambda_{\text{aux}} \mathcal{L}_{\text{aux}} + \lambda_{\text{reproj}} \mathcal{L}_{\text{reproj}}, \quad (7)$$

where \mathcal{L}_{aux} enforces alignment between GT and predicted auxiliary 2D keypoints, and $\mathcal{L}_{\text{reproj}}$ minimizes reprojection error between GT 2D and projected 3D keypoints, both using L_1 loss. By restricting optimization to a small parameter subset and a few steps, TTA remains stable and efficient while correcting pose misalignment and articulation errors. Notably, for fair comparisons, the proposed TTA is employed exclusively during Stage 2 for pGT generation, and is not utilized in Stage 1 or Stage 3 for comparative evaluation.

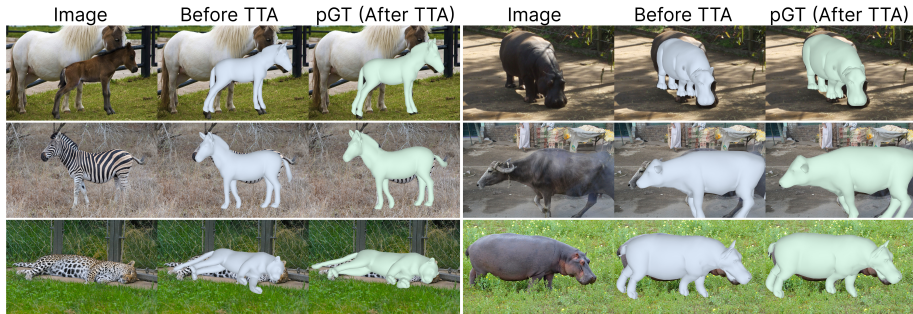


Fig. 4: **Quadruped3D pGT examples.** Each row visualizes the input image (left), the initial 3D prediction before test-time adaptation (middle), and the refined pGT after adaptation (right), illustrating pose alignment and shape recovery across diverse species and articulated poses.

3.5 Our Quadruped3D Dataset

Quadruped2D curation. Quadruped2D is constructed from the SuperAnimal dataset [50], which contains 80k images of quadruped animals. From this dataset, we sample 24k images spanning 23 animal species, while preserving the original SuperAnimal train–test split, yielding a 6:4 ratio in our subset.

Fidelity-Aware Pseudo-GT Construction. Based on the Quadruped2D dataset, we introduce a reprojection-driven confidence control strategy to construct reliable 3D pGT. Rather than refining all samples indiscriminately, we use our pre-trained model to assess the initial reconstruction quality over the unlabeled 14K 2D training pool in Quadruped2D to construct Quadruped3D.

Each instance is evaluated according to its initial 2D reprojection error \mathcal{L}_{proj} and its optimization behavior. We define two reprojection error thresholds τ_{low} and τ_{high} to partition the samples based on reconstruction confidence. Samples with $\mathcal{L}_{proj} < \tau_{low}$ are directly retained, as their predictions already exhibit stable geometric alignment. For instances with moderate reprojection error ($\tau_{low} \leq \mathcal{L}_{proj} < \tau_{high}$), we apply test-time optimization to further improve reconstruction quality. Samples with large initial reprojection error ($\mathcal{L}_{proj} \geq \tau_{high}$) or negligible optimization improvement (i.e., $\Delta\mathcal{L}_{proj} < \delta$ within 10 iterations) are discarded.

Applying this quality-controlled refinement pipeline to the 14K annotated training images yields 9K high-confidence 3D pGT samples. Among them, 5K are directly retained without refinement, while 4K are improved through test-time adaptation. The resulting pGT set achieves an overall average AUC of 94.0. Fig. 4 shows representative examples of the curated 3D pGT. The refined meshes demonstrate accurate pose alignment and plausible shape consistency across diverse viewpoints and challenging articulations, validating the effectiveness of our quality-controlled pseudo-label generation framework.

4 Experiments

4.1 Datasets

The proposed framework facilitates the integration of a wide range of animal datasets comprising both 2D and 3D annotations. In the training stage-1, we jointly utilize the Animal3D [46], CtrlAni3D [28], and Quadruped2D [50] datasets. In training stage-3, the network is trained from scratch on the Animal3D [46], CtrlAni3D [28], and our Quadruped3D datasets, with pGT generated on a per-case basis from stage-2. The Animal Kingdom [50] dataset is employed to evaluate out-of-distribution generalization performance.

4.2 Metrics

We evaluate model performance using both 3D and 2D metrics. For 3D evaluation, we report PA-MPJPE (hereafter abbreviated as PAJ), defined as the Procrustes-aligned mean per-joint position error, and PA-MPVPE (hereafter abbreviated as PAV), defined as the Procrustes-aligned mean per-vertex position error computed over the SMAL mesh vertices. For 2D evaluation, we use PCK (Percentage of Correct Keypoints), measuring the proportion of predicted keypoints within a given threshold of the ground truth. We report PCK@0.1 and PCK@0.15 (denoted P@0.1 and P@0.15 in tables). Additionally, we report AUC (Area Under the Curve), obtained by integrating PCK over thresholds from 0 to 1. Notably, both the 2D and 3D keypoints employed for metric computation are derived from the predicted mesh. To evaluate whether the predicted animal shapes capture meaningful family-level structure, we compute the Adjusted Rand Index (ARI) between the clustering results and ground-truth family labels. ARI measures similarity between two partitions while correcting for chance, ranging from -1 to 1, with 1 indicating perfect alignment and 0 corresponding to random assignment.

4.3 Implementation Details

We implement the network in PyTorch. For the image encoder, we initialize the ViT with pre-trained weights from AniMer [1], which has been previously trained on the mesh recovery task. For the BioCLIP [41] embeddings, we employ the vit_b16_pn_bioclip-v1 model. We adopt different learning rates for the encoder and the remaining network components: the encoder is optimized with a learning rate of 3.75×10^{-7} , while the remaining parameters use a learning rate of 3.75×10^{-6} . The networks are trained for 1200 epochs, at which point the training loss is observed to stabilize. We use a batch size of 48 and optimize the parameters with the AdamW optimizer [27], combined with a linear learning rate decay schedule. Additional model architecture details are in the Supplement.

4.4 Comparison with State-of-the-Art Methods

Following the evaluation protocols of Animal3D [46] and AniMer+ [1], we quantitatively compare our model with several baselines, including HMR [17], HMR2.0 [12], GenZoo [33], WLDO [4], AniMer [28], and AniMer+ [1]. Since GenZoo is trained with the SMAL+ [55] model, we limit our evaluation to 26 3D joints

and 2D metrics. For qualitative comparisons, we focus on AniMer and AniMer+, as these methods also address multi-species mesh recovery tasks.

As shown in Tab. 1, our model achieves state-of-the-art performance on two 3D datasets across both 3D and 2D evaluation metrics. Furthermore, as reported in Tab. 2, our approach maintains SOTA performance on the challenging out-of-domain Animal Kingdom test dataset.

The qualitative results in Fig. 5 further highlight the advantages of our approach. Overall, the meshes predicted by our model exhibit better alignment across major body parts, including the legs, tail, and head. Moreover, our method more accurately preserves the characteristic shape of the correct animal family compared to the baselines. More qualitative comparisons are provided in the Supplement.

For example, in the first row, AniMer and AniMer+ predict a dog-like shape given a zebra input. Similarly, in the fourth row (sheep), both baseline methods produce predictions resembling a Felidae-like family, whereas our model successfully captures the distinctive sheep-like shape. Additional qualitative results are provided in the Supplementary Material. To quantify shape prediction, we use t-SNE [29] to visualize the predicted and GT shape parameters on the Animal3D test set. As shown in Fig. 6, our method produces compact and well-separated clusters that closely resemble the GT distribution. In contrast, AniMer [28] and AniMer+ [1] exhibit more dispersed embeddings with noticeable cluster overlap and outliers. This observation is consistent with the ARI scores. Our method achieves an ARI of 0.98, approaching the GT clustering score (0.99), and significantly outperforming AniMer (0.82) and AniMer+ (0.61), indicating substantially better alignment with the underlying shape categories.

Method	Animal3D			CtrlAni3D		
	AUC↑	PAJ↓	PAV↓	AUC↑	PAJ↓	PAV↓
HMR [17]	76.3	123.5	133.9	80.8	123.5	133.9
WLDO [4]	78.2	112.3	125.2	88.7	71.5	83.4
HMR2.0 [12]	86.7	94.1	98.5	91.8	60.9	66.4
GenZoo [33]	86.6	138.5	-	92.9	116.4	-
AniMer [28]	88.9	80.4	85.7	93.8	44.1	47.6
AniMer+ [1]	88.9	78.0	82.7	93.6	47.8	50.8
Ours (Stage-1)	<u>89.6</u>	<u>75.3</u>	<u>79.5</u>	<u>94.0</u>	<u>40.1</u>	<u>42.8</u>
Ours (Stage-3)	89.9	74.7	79.4	94.2	40.1	42.7

Table 1: Quantitative comparison on 3D datasets: Animal3D and CtrlAni3D. **Bold**: best. Underline: second best.

Method	Quadruped2D			Animal Kingdom		
	AUC↑	P@0.1↑	P@0.15↑	AUC↑	P@0.1↑	P@0.15↑
AniMer [28]	87.6	63.8	78.6	82.9	34.9	54.7
AniMer+ [1]	86.7	60.7	76.8	82.6	34.2	53.0
Ours (Stage-1)	<u>92.0</u>	<u>79.8</u>	<u>90.0</u>	83.9	38.9	57.8
Ours (Stage-3)	92.5	83.5	91.1	<u>83.7</u>	<u>37.8</u>	<u>57.3</u>

Table 2: Quantitative comparison on 2D datasets: Quadruped2D and Animal Kingdom. **Bold**: best. Underline: second best.

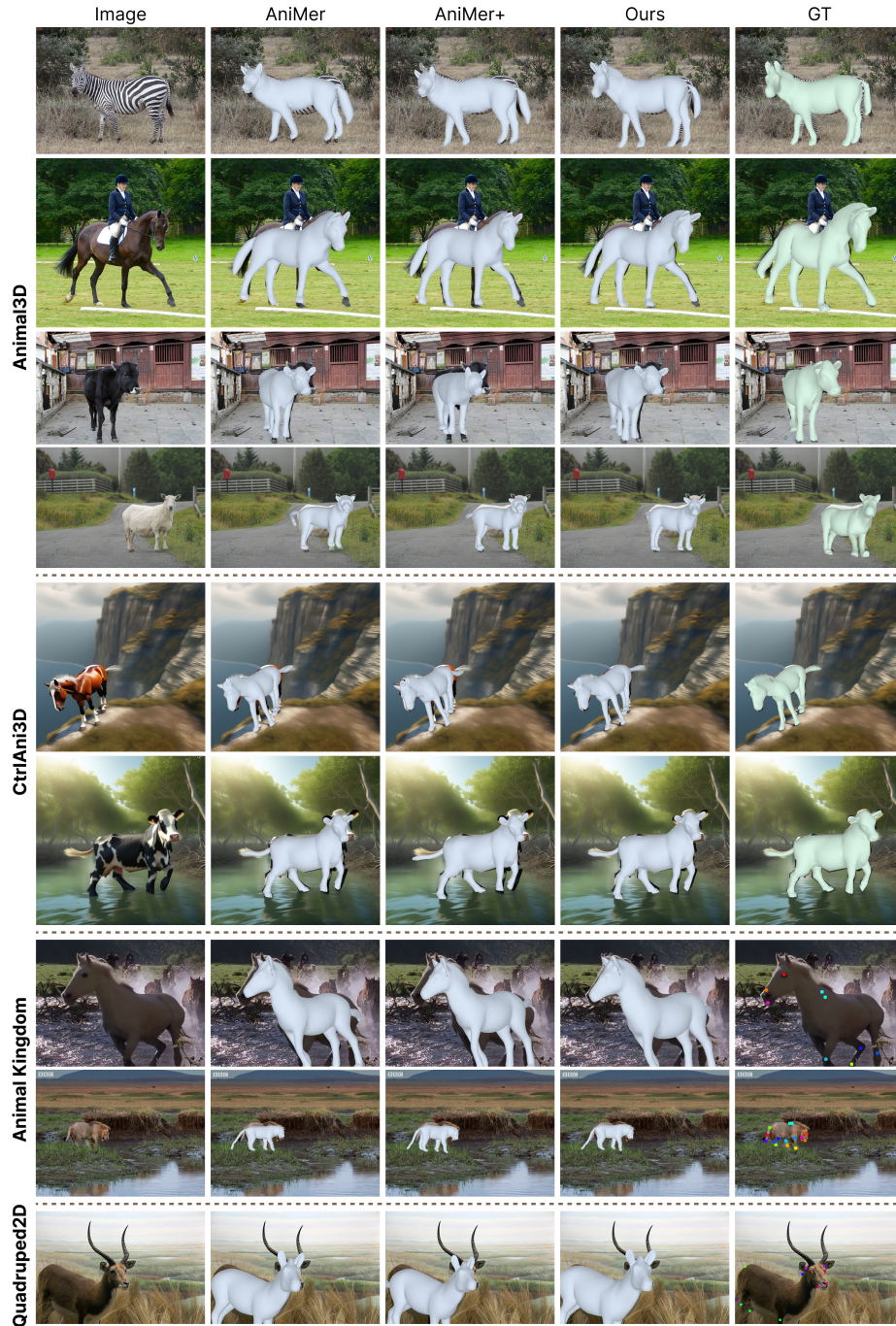


Fig. 5: Qualitative comparisons on Animal3D (rows 1–4), CtrlAni3D (rows 5–6), Animal Kingdom (rows 7–8), and Quadruped2D (row 9) datasets. We compare our results with AniMer [28] and AniMer+ [1]

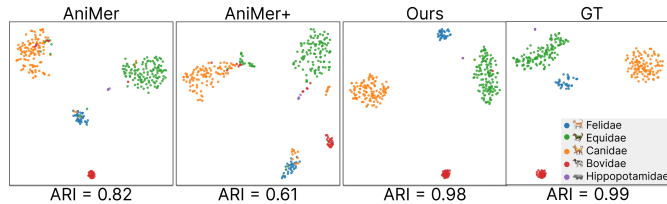


Fig. 6: t-SNE [29] embeddings of predicted and GT shape parameters on Animal3D. Colors indicate different animal family category labels.

4.5 Ablation Study

Ablation on model architecture. We assess the contribution of biological priors and learnable keypoint tokens through three ablation variants. (a) w/o F_{bio} : We remove biologically initialized shape features while retaining the coarse-to-fine shape estimation strategy. For fair comparison, we replace the BioCLIP embedding model with a randomly initialized learnable encoder. (b) w/o β_{init} : We discard biologically initialized shape parameters and instead initialize the shape coefficients to zero. (c) w/o T_{keypoint} : We remove learnable keypoint tokens, so that pose and shape are directly regressed from the SMAL parameter token.

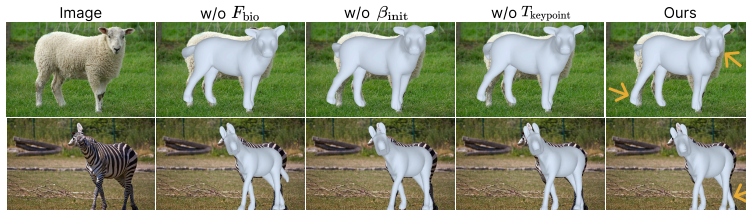


Fig. 7: **Ablation on model architecture.** The top row shows a sheep from Quadruped2D, and the bottom row shows a zebra from Animal3D.

Method	Animal3D		CtrlAni3D		Quadruped2D		Animal Kingdom	
	PAJ↓	PAV↓	PAJ↓	PAV↓	AUC↑	P@0.1↑	AUC↑	P@0.1↑
w/o F_{bio}	75.5	79.7	43.5	46.2	91.7	78.5	83.6	37.3
w/o β_{init}	75.6	80.1	41.8	44.4	91.9	78.9	83.4	36.1
w/o T_{keypoint}	75.6	80.2	43.5	46.2	91.1	75.9	83.7	37.0
Ours (Stage-1)	75.3	79.5	40.1	42.8	92.0	79.8	83.9	38.9

Table 3: **Effect of biological priors and learnable keypoint tokens.** All models presented are trained on the combined Animal3D, CtrlAni3D, and Quadruped2D datasets under identical training configurations.

As reported in Tab. 3, removing keypoint tokens or biological priors degrades both 2D reprojection accuracy and 3D mesh reconstruction quality. Qualitative results in Fig. 7 show that incorporating them leads to more accurate and stable poses, with improved shape details such as facial features for the sheep and limb poses for the zebra. To further validate biological embedding, we analyze the

t-SNE visualization of the bio-token and init shape feature with and without F_{bio} in the Supplement.

Ablation on test-time adaptation. To demonstrate the effect of our proposed TTA, we focus on high-error cases from the Animal3D dataset, as shown in Fig. 8. These cases typically involve out-of-domain poses and significant self-occlusion, highlighting the challenges addressed by our method. Quantitative comparisons before and after TTA are reported in Tab. 4. Except for the 3D metrics in the cat-licking case, all cases show improvements in both 2D and 3D. The 3D drop for cat licking is caused by misalignment between the 3D ground-truth mesh and the annotated 2D keypoints, as indicated by the low AUC in pGT.

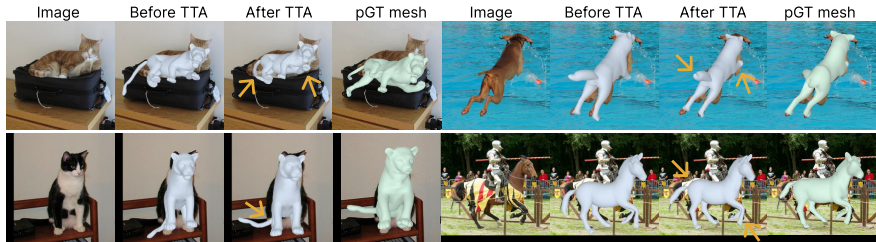


Fig. 8: **Qualitative results on Animal3D dataset before and after test-time adaptation.** The orange arrow indicates better alignment refined after TTA compared to before.

Instance	PAJ↓		PAV↓		AUC↑		
	Before	After	Before	After	Before	After	pGT
Cat licking	273.6	313.9	295.8	318.1	<u>83.5</u>	92.6	81.6
Dog jumping	133.1	117.6	114.2	80.6	81.9	90.1	95.8
Cat sitting	113.6	88.3	77.2	67.2	86.5	94.6	91.8
Horse running	52.1	46.0	53.2	52.9	90.5	93.7	95.3
Avg over Animal3D	75.3	71.7	79.5	75.9	89.6	91.5	92.7

Table 4: Quantitative comparison of model performance before and after TTA on four specific cases and on the overall average in the Animal3D dataset. **Bold** indicates improvement after TTA. Underline indicates performance surpassing pGT in terms of 2D reprojection accuracy (AUC).

5 Conclusions

We present PRIMA, a framework for high-fidelity 3D mesh recovery of animals that combines biological priors, test-time adaptation, and large-scale pseudo-3D data. By leveraging BioCLIP embeddings and TTA, PRIMA achieves accurate and generalizable shape and pose predictions, even for underrepresented species and challenging poses. The automatically constructed Quadruped3D dataset further enables systematic model improvement and serves as a valuable benchmark, advancing the state-of-the-art performance on various benchmarks in both 2D alignment and 3D reconstruction.

References

1. An, L., Lyu, J., Lin, L., Cheng, P., Liu, Y., Tang, X.: Animer+: Unified pose and shape estimation across mammalia and aves via family-aware transformer. *IEEE Transactions on Pattern Analysis and Machine Intelligence* (2025)
2. Badger, M., Wang, Y., Modh, A., Perkes, A., Kolotouros, N., Pfrommer, B.G., Schmidt, M.F., Danilidis, K.: 3d bird reconstruction: a dataset, model, and shape recovery from a single view. In: *ECCV*. pp. 1–17. Springer (2020)
3. Bidulka, L., Gholami, M., Zheng, J., McKeown, M.J., Wang, Z.J.: Escape: Energy-based selective adaptive correction for out-of-distribution 3d human pose estimation. *Neurocomputing* **611**, 128605 (2025)
4. Biggs, B., Boyne, O., Charles, J., Fitzgibbon, A., Cipolla, R.: Who left the dogs out? 3d animal reconstruction with expectation maximization in the loop. In: *ECCV*. pp. 195–211. Springer (2020)
5. Biggs, B., Roddick, T., Fitzgibbon, A., Cipolla, R.: Creatures great and SMAL: Recovering the shape and motion of animals from video. In: *ACCV* (2018)
6. Bogo, F., Kanazawa, A., Lassner, C., Gehler, P., Romero, J., Black, M.J.: Keep it smpl: Automatic estimation of 3d human pose and shape from a single image. In: *ECCV*. pp. 561–578 (2016)
7. Cho, G., Kang, C., Soon, D., Joo, K.: Dogrecon: Canine prior-guided animatable 3d gaussian dog reconstruction from a single image: G. cho et al. *International Journal of Computer Vision* **133**(9), 6332–6346 (2025)
8. Dwivedi, S.K., Sun, Y., Patel, P., Feng, Y., Black, M.J.: Tokenhmr: Advancing human mesh recovery with a tokenized pose representation. In: *CVPR*. pp. 1323–1333 (2024)
9. Fang, Q., Shuai, Q., Dong, J., Bao, H., Zhou, X.: Reconstructing 3d human pose by watching humans in the mirror. In: *CVPR* (2021)
10. Ferguson, A., Osman, A.A., Bescos, B., Stoll, C., Twigg, C., Lassner, C., Otte, D., Vignola, E., Prada, F., Bogo, F., et al.: Mhr: Momentum human rig. *arXiv preprint arXiv:2511.15586* (2025)
11. Goel, S., Pavlakos, G., Rajasegaran, J., Kanazawa, A., Malik, J.: Humans in 4d: Reconstructing and tracking humans with transformers. In: *ICCV*. pp. 14783–14794 (2023)
12. Goel, S., Pavlakos, G., Rajasegaran, J., Kanazawa, A., Malik, J.: Humans in 4d: Reconstructing and tracking humans with transformers. In: *ICCV*. pp. 14783–14794 (2023)
13. Gu, J., Stevens, S., Campolongo, E.G., Thompson, M.J., Zhang, N., Wu, J., Kopanav, A., Mai, Z., White, A.E., Balhoff, J., et al.: Bioclip 2: Emergent properties from scaling hierarchical contrastive learning. *arXiv preprint arXiv:2505.23883* (2025)
14. Guan, S., Xu, J., He, M.Z., Wang, Y., Ni, B., Yang, X.: Out-of-domain human mesh reconstruction via dynamic bilevel online adaptation. *IEEE Transactions on Pattern Analysis and Machine Intelligence* (2022)
15. Ionescu, C., Papava, D., Olaru, V., Sminchisescu, C.: Human3.6m: Large scale datasets and predictive methods for 3D human sensing in natural environments. *IEEE Transactions on Pattern Analysis and Machine Intelligence* **36**(7), 1325–1339 (2013)
16. Joo, H., Neverova, N., Vedaldi, A.: Exemplar fine-tuning for 3D human model fitting towards in-the-wild 3D human pose estimation. In: *3DV*. pp. 42–52. *IEEE* (2021)

17. Kanazawa, A., Black, M.J., Jacobs, D.W., Malik, J.: End-to-end recovery of human shape and pose. In: CVPR. pp. 7122–7131 (2018)
18. Kanazawa, A., Tulsiani, S., Efros, A.A., Malik, J.: Learning category-specific mesh reconstruction from image collections. In: ECCV. pp. 371–386 (2018)
19. Kulits, P., Black, M.J., Zuffi, S.: Reconstructing animals and the wild. In: CVPR. pp. 16565–16577 (June 2025)
20. Kulkarni, N., Gupta, A., Fouhey, D.F., Tulsiani, S.: Articulation-aware canonical surface mapping. In: CVPR. pp. 452–461 (2020)
21. Li, C., Lee, G.H.: Coarse-to-fine animal pose and shape estimation. *Advances in Neural Information Processing Systems* **34**, 11757–11768 (2021)
22. Li, C., Ghorbani, N., Broomé, S., Rashid, M., Black, M.J., Hernlund, E., Kjellström, H., Zuffi, S.: hsmal: Detailed horse shape and pose reconstruction for motion pattern recognition. *arXiv preprint arXiv:2106.10102* (2021)
23. Li, C., Yang, Y., Weng, Z., Hernlund, E., Zuffi, S., Kjellström, H.: Dessie: Disentanglement for articulated 3d horse shape and pose estimation from images. In: *Proceedings of the Asian Conference on Computer Vision*. pp. 764–783 (2024)
24. Li, Z., Amrani, A., Rai, S., Laga, H.: Advances and trends in the 3d reconstruction of the shape and motion of animals. *arXiv preprint arXiv:2508.16062* (2025)
25. Li, Z., Litvak, D., Li, R., Zhang, Y., Jakab, T., Rupperecht, C., Wu, S., Vedaldi, A., Wu, J.: Learning the 3d fauna of the web. In: CVPR. pp. 9752–9762 (2024)
26. Loper, M., Mahmood, N., Romero, J., Pons-Moll, G., Black, M.J.: SMPL: A skinned multi-person linear model. *ACM TOG* **34**(6), 1–16 (2015)
27. Loshchilov, I., Hutter, F.: Decoupled weight decay regularization. *arXiv preprint arXiv:1711.05101* (2017)
28. Lyu, J., Zhu, T., Gu, Y., Lin, L., Cheng, P., Liu, Y., Tang, X., An, L.: Animer: Animal pose and shape estimation using family aware transformer. In: CVPR. pp. 17486–17496 (2025)
29. Van der Maaten, L., Hinton, G.: Visualizing data using t-sne. *Journal of machine learning research* **9**(11) (2008)
30. Mahmood, N., Ghorbani, N., Troje, N.F., Pons-Moll, G., Black, M.J.: AMASS: Archive of motion capture as surface shapes. In: ICCV. pp. 5442–5451 (Oct 2019)
31. Mu, J., Qiu, W., Hager, G.D., Yuille, A.L.: Learning from synthetic animals. In: CVPR (June 2020)
32. Nam, H., Jung, D.S., Oh, Y., Lee, K.M.: Cyclic test-time adaptation on monocular video for 3d human mesh reconstruction. In: ICCV. pp. 14829–14839 (2023)
33. Niewiadomski, T., Yiannakidis, A., Cuevas-Velasquez, H., Sanyal, S., Black, M.J., Zuffi, S., Kulits, P.: Generative zoo. In: ICCV. pp. 8492–8502 (2025)
34. Pavlakos, G., Choutas, V., Ghorbani, N., Bolkart, T., Osman, A.A., Tzionas, D., Black, M.J.: Expressive body capture: 3d hands, face, and body from a single image. In: CVPR. pp. 10975–10985 (2019)
35. Pavlakos, G., Shan, D., Radosavovic, I., Kanazawa, A., Fouhey, D., Malik, J.: Reconstructing hands in 3d with transformers. In: CVPR. pp. 9826–9836 (2024)
36. Peng, S., Zhang, Y., Xu, Y., Wang, Q., Shuai, Q., Bao, H., Zhou, X.: Neural body: Implicit neural representations with structured latent codes for novel view synthesis of dynamic humans. In: CVPR (2021)
37. Rempe, D., Birdal, T., Hertzmann, A., Yang, J., Sridhar, S., Guibas, L.J.: Humor: 3d human motion model for robust pose estimation. In: ICCV. pp. 11488–11499 (2021)
38. Rueegg, N., Zuffi, S., Schindler, K., Black, M.J.: Barc: Learning to regress 3d dog shape from images by exploiting breed information. In: CVPR. pp. 3876–3884 (2022)

39. Rüegg, N., Tripathi, S., Schindler, K., Black, M.J., Zuffi, S.: Bite: Beyond priors for improved three-d dog pose estimation. In: CVPR. pp. 8867–8876 (2023)
40. Sabathier, R., Mitra, N.J., Novotny, D.: Animal avatars: Reconstructing animatable 3d animals from casual videos. In: ECCV. pp. 270–287. Springer (2024)
41. Stevens, S., Wu, J., Thompson, M.J., Campolongo, E.G., Song, C.H., Carlyn, D.E., Dong, L., Dahdul, W.M., Stewart, C., Berger-Wolf, T., Chao, W.L., Su, Y.: Bio-CLIP: A vision foundation model for the tree of life. In: CVPR. pp. 19412–19424 (2024)
42. Tan, J., Yang, G., Ramanan, D.: Distilling neural fields for real-time articulated shape reconstruction. In: CVPR. pp. 4692–4701 (2023)
43. Wang, T., Liu, M., Liu, H., Ren, B., You, Y., Li, W., Sebe, N., Li, X.: Uncertainty-aware testing-time optimization for 3d human pose estimation. *IEEE Transactions on Multimedia* (2026)
44. Wang, Y., Kolotouros, N., Daniilidis, K., Badger, M.: Birds of a feather: Capturing avian shape models from images. In: CVPR. pp. 14739–14749 (2021)
45. Wu, J., Pavlakos, G., Gkioxari, G., Malik, J.: Reconstructing hand-held objects in 3d from images and videos. arXiv preprint arXiv:2404.06507 (2024)
46. Xu, J., Zhang, Y., Peng, J., Ma, W., Jesslen, A., Ji, P., Hu, Q., Zhang, J., Liu, Q., Wang, J., et al.: Animal3d: A comprehensive dataset of 3d animal pose and shape. In: ICCV. pp. 9099–9109 (2023)
47. Yang, X., Kukreja, D., Pinkus, D., Sagar, A., Fan, T., Park, J., Shin, S., Cao, J., Liu, J., Ugrinovic, N., Feiszli, M., Malik, J., Dollar, P., Kitani, K.: Sam 3d body: Robust full-body human mesh recovery. arXiv preprint arXiv:2602.15989 (2026)
48. Yao, C.H., Hung, W.C., Li, Y., Rubinstein, M., Yang, M.H., Jampani, V.: Lassie: Learning articulated shapes from sparse image ensemble via 3d part discovery. *Advances in Neural Information Processing Systems* **35**, 15296–15308 (2022)
49. Yao, C.H., Hung, W.C., Li, Y., Rubinstein, M., Yang, M.H., Jampani, V.: Hi-lassie: High-fidelity articulated shape and skeleton discovery from sparse image ensemble. In: CVPR. pp. 4853–4862 (2023)
50. Ye, S., Filippova, A., Lauer, J., Schneider, S., Vidal, M., Qiu, T., Mathis, A., Mathis, M.W.: Superanimal pretrained pose estimation models for behavioral analysis. *Nature communications* **15**(1), 5165 (2024)
51. You, Y., Liu, H., Wang, T., Li, W., Ding, R., Li, X.: Co-evolution of pose and mesh for 3d human body estimation from video. In: ICCV. pp. 14963–14973 (2023)
52. Zhang, J., Nie, X., Feng, J.: Inference stage optimization for cross-scenario 3D human pose estimation. In: NeurIPS. pp. 2408–2419 (2020)
53. Zheng, Z., Yu, T., Wei, Y., Dai, Q., Liu, Y.: Deephuman: 3d human reconstruction from a single image. In: ICCV (October 2019)
54. Ziouliis, N., O’Brien, J.F.: Kbody: Towards general, robust, and aligned monocular whole-body estimation. In: CVPR. pp. 6215–6225 (2023)
55. Zuffi, S., Black, M.J.: Awol: Analysis without synthesis using language. In: ECCV. pp. 1–19. Springer (2024)
56. Zuffi, S., Kanazawa, A., Berger-Wolf, T., Black, M.J.: Three-d safari: Learning to estimate zebra pose, shape, and texture from images” in the wild”. In: ICCV. pp. 5359–5368 (2019)
57. Zuffi, S., Kanazawa, A., Jacobs, D., Black, M.J.: 3D menagerie: Modeling the 3D shape and pose of animals. In: CVPR (Jul 2017)
58. Zuffi, S., Mellbin, Y., Li, C., Hoeschle, M., Kjellström, H., Polikovsky, S., Hernlund, E., Black, M.J.: Varen: Very accurate and realistic equine network. In: CVPR. pp. 5374–5383 (2024)

PRIMA: Boosting Animal Mesh Recovery with Biological Priors and Test-Time Adaptation

Supplementary Material

A Dataset Statistics: Taxonomic Distribution

To characterize the imbalance of animal categories in existing datasets, we analyze the taxonomic distribution of the existing datasets. First, we examine the distribution of samples at the family level. Fig. 1 shows the number of instances for five animal families in three widely used datasets, Animal3D [46], CtrlAni3D [28], and Quadruped2D [50]. As illustrated in the figure, the distribution across families is highly uneven, with Equidae and Canidae dominating the dataset while others contain substantially fewer samples. This imbalance suggests that current datasets may bias learning algorithms toward more frequently observed animal families.

We further analyze the distribution at the species level using the Animal3D [46] dataset. As shown in Fig. 2, the dataset contains 40 animal species, but the number of samples per species varies significantly. The resulting distribution exhibits a long-tailed pattern, where a small subset of species accounts for the majority of samples, while many species have relatively few instances. Such an imbalance may hinder the learning of robust and generalizable animal representations.

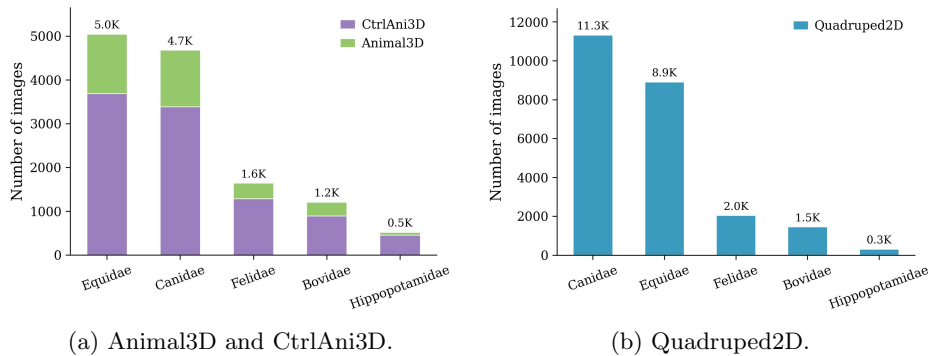


Fig. 1: Family-level image distributions of the datasets used in this work.

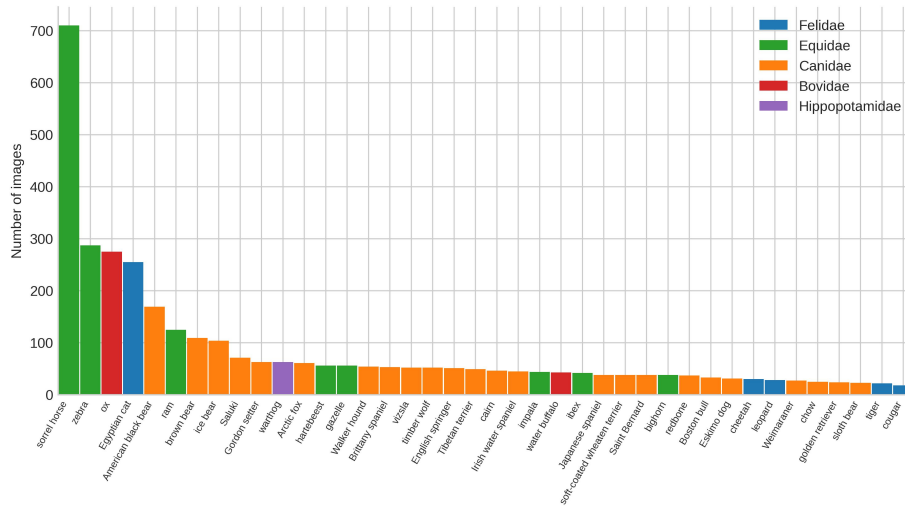


Fig. 2: **Species-level image distribution of the Animal3D dataset across 40 categories, sorted by total count in descending order.** Bar colors indicate the biological family: **Felidae**, **Equidae**, **Canidae**, **Bovidae**, and **Hippopotamidae**. The dataset contains 3,385 images in total and exhibits significant class imbalance, with the most populated category (*sorrel horse*, 710 images) containing $\sim 39\times$ more images than the least populated (*cougar*, 18 images).

B Additional Implementation Details

B.1 Details of network training

For the bio-encoder, the dimensionality of the biological feature representation is 768. These features are subsequently projected to a 1280-dimensional bio-token space. The ViT encoder extracts visual representations, producing a sequence of feature tokens of size 192×1280 . For the keypoint-aware decoder, we employ an Iterative Error Feedback (IEF) loop to progressively refine the SMAL parameters. In our configuration, we perform $N = 3$ Iterative Error Feedback (IEF) iterations during the warm-up phase, and, in order to improve computational efficiency, we reduce the number of iterations to $N = 1$ in the subsequent phase. Between consecutive decoder iterations, we insert $L = 6$ transformer layers. At each transformer layer, both the 2D and 3D keypoint estimates are iteratively refined.

During the initial warm-up training phase, the network is pre-trained exclusively on the Animal3D dataset for 500 epochs to encourage the learning of plausible shapes and poses. Subsequently, the full set of training data is introduced for further training. The overall training time is 46 hours.

B.2 Details of test-time adaptation

Our test-time adaptation (TTA) approach optimizes the SMAL parametric model’s shape and pose parameters using only ground-truth 2D keypoint annotations available at test time. TTA adapts the predicted SMAL parameters for each test sample through a lightweight optimization procedure.

During TTA, we optimize approximately 4.5M parameters within the SMAL regression head, including learnable query tokens and regression MLPs for shape, pose, and camera parameters. The optimization is performed using the Adam optimizer with a learning rate of 1×10^{-6} for 10 to 60 iterations per sample, depending on the baseline performance. The TTA objective focuses on SMAL-reconstructed and auxiliary 2D keypoints, ensuring gradients effectively reach shape and pose parameters. The loss weights are set to:

$$\lambda_{\text{aux}} = 5.0, \quad \lambda_{\text{reproj}} = 0.5. \quad (\text{A})$$

In terms of runtime, baseline inference takes approximately 0.05 s per image on an NVIDIA A100 GPU. With TTA enabled, the runtime increases to approximately 0.35 s per image for 10 optimization iterations.

C Additional Results

C.1 Qualitative comparisons with state-of-the-art methods

We present additional qualitative comparisons with SOTA methods on the Animal3D and the Quadruped2D dataset. As shown in Fig. 3, the first four rows depict instances from the Bovidae family. In these examples, other SOTA methods hallucinate shapes resembling canines, whereas our approach more faithfully reconstructs bovine morphology. Row 5 shows a sheep example: AniMer captures overall body shape but has less accurate pose, while AniMer+ incorrectly predicts a feline-like geometry. In row 6, only our method reconstructs a shape consistent with the appearance of a bear. Similarly, in the Quadruped2D dataset, our results show a closer alignment between shape and animal species.

C.2 Family-wise quantitative comparisons

To assess method performance across varying morphologies, we perform family-wise comparisons on the Animal3D dataset. Tab. 1 presents family-wise quantitative comparisons on the Animal3D dataset across five animal families. Overall, our method demonstrates strong and consistent performance across categories, achieving the best PA-MPJPE results in four families (Equidae, Canidae, Felidae, and Bovidae).

Comparing the two stages of our method, Stage-3 further improves PAJ across most categories compared with Stage-1, showing that the refinement stage effectively enhances pose estimation accuracy. In terms of PAV, our method achieves the best results for Felidae and Bovidae, and remains competitive for

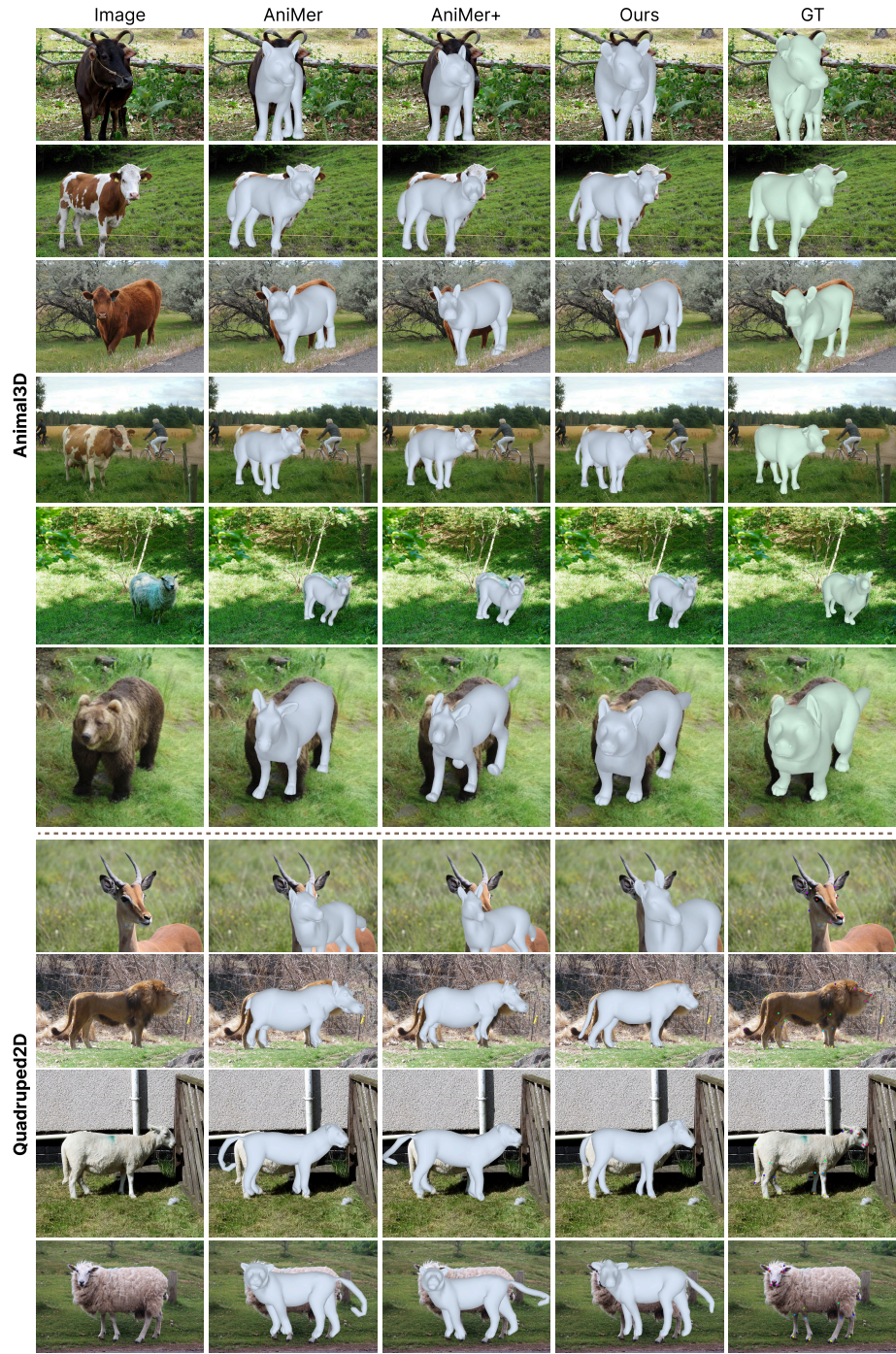


Fig. 3: Qualitative comparisons on Animal3D and Quadruped2D dataset.

C.4 More qualitative results on Animal Kingdom dataset

We present qualitative results on the Animal Kingdom dataset, which consists of challenging in-the-wild imagery. As illustrated in Fig. 5, PRIMA exhibits consistently robust performance even under challenging imaging conditions, including occlusions (second example in the first row), motion blur (first example in the fourth row), and artifacts induced by camera traps (first example in the second row).

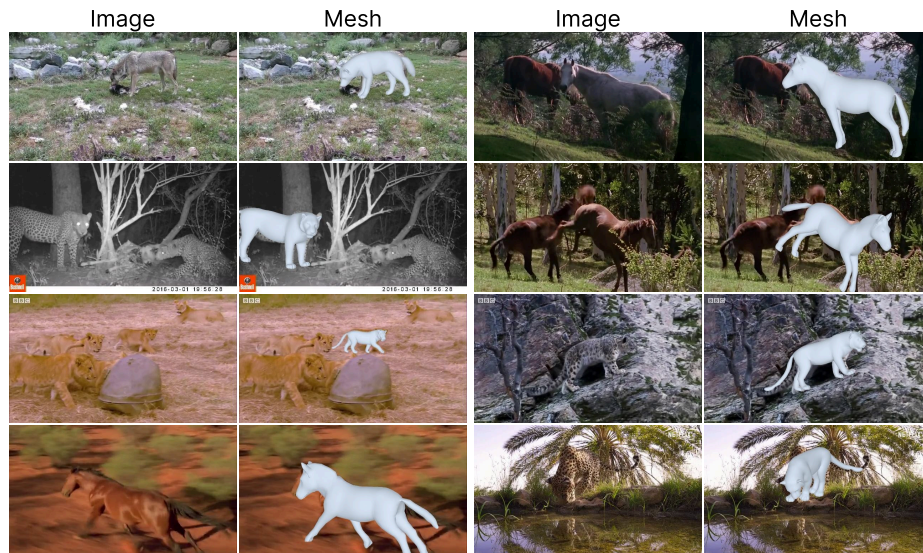


Fig. 5: Qualitative results on Animal Kingdom datasets.

D Additional Ablation Study

D.1 Ablation on biological priors

To validate the biological embedding, we analyze the t-SNE [29] visualizations of the BioCLIP [41] feature and the shape init features, both with and without F_{bio} . As shown in Fig. 6, when employing the F_{bio} encoder, the BioCLIP feature already encodes species-specific information within the image feature space, with ARI being 0.365, and the shape initialization feature becomes more closely aligned with the corresponding species clusters. In contrast, in the absence of F_{bio} , the feature space of the BioCLIP embeddings appears more dispersed and lacks a clear cluster structure.

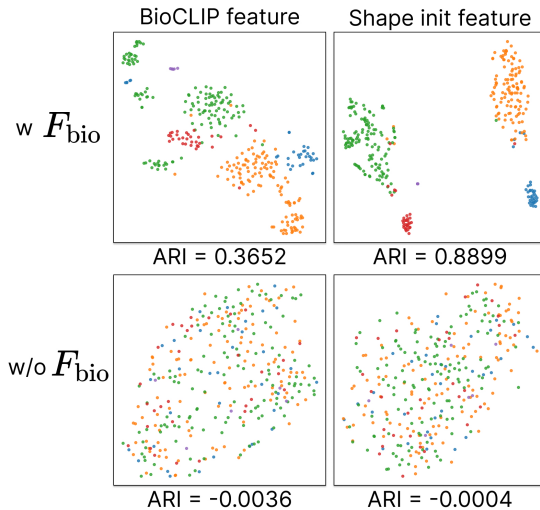


Fig. 6: t-SNE [29] visualization of BioCLIP feature and shape init feature on the Animal3D test set.

D.2 Ablation on Quadruped3D

To further demonstrate the impact of our Quadruped3D dataset, we conduct a comparative analysis between stage-1 and stage-3 training regimes, in which the model is trained with Quadruped2D and Quadruped3D, respectively, along with the Animal3D and CtrlAni3D datasets. As shown in Fig. 7, training with Quadruped3D yields better limb alignment in Animal3D and Animal Kingdom, and overall alignment improves when the animal is close and partially visible, as in the lion example in the last row.

D.3 Ablation on test-time adaptation.

We analyze the influence of optimization iterations on the test-time adaptation (TTA) performance using the horse-running scenario as a case study. We report results in terms of the relative improvement with respect to the baseline obtained without adaptation (i.e., 0 optimization steps). For error metrics (PA-MPJPE and PA-MPVPE), the improvement corresponds to the relative error reduction compared to the baseline, while for AUC it represents the relative increase over the baseline.

As shown in the left panel of Fig. 8, increasing the number of optimization iterations consistently improves PA-MPJPE and AUC, indicating that TTA helps refine the pose estimation by better aligning the 3D prediction with the 2D observations. In contrast, PA-MPVPE increases initially and reaches its maximum at around 15 optimization steps, after which the performance gradually degrades. When the number of optimization iterations grows large (around 70

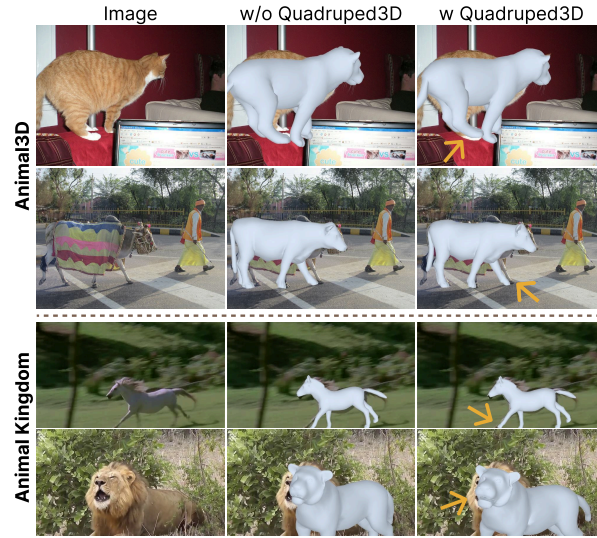


Fig. 7: Effect of training with Quadruped3D on Animal3D (rows 1-2), and Animal Kingdom (rows 3-4) datasets.

steps), performance degrades and even drops below the no-adaptation baseline. This suggests that excessive optimization overfits the 2D observations and degrades mesh reconstruction, especially without using silhouette information, unlike the SMALify [5] optimization process.

We also investigate how the number of 2D keypoints influences the TTA. In the horse-running scenario, the original annotation provides 22 visible keypoints. To evaluate the robustness to keypoint sparsity, we randomly mask 30%, 50%, and 70% of the keypoints, resulting in 16, 11, and 7 visible keypoints, respectively. The right panel of Fig. 8 shows the PA-MPVPE improvement across different visible keypoint conditions. The number of available keypoints significantly affects the stability of the adaptation process. When sufficient keypoints are available, a small number of optimization steps leads to moderate performance gains, while excessive iterations gradually degrade the results. In contrast, when only 7 keypoints are visible, the performance quickly deteriorates as the number of iterations increases. These results show that dense, reliable keypoint observations are crucial for stable, effective test-time adaptation.

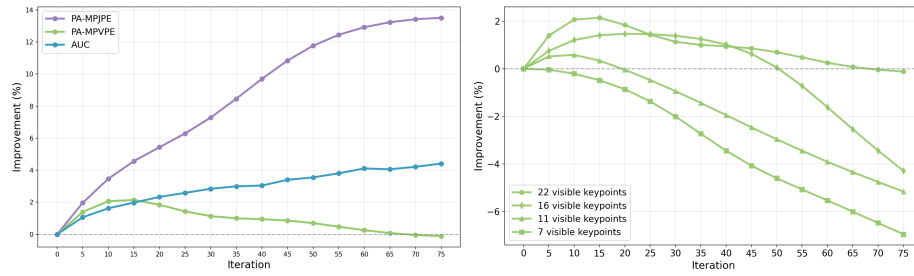


Fig. 8: **Effect of optimization iterations and visible keypoints in the horse-running case.** Left: Relative improvement of PA-MPJPE, PA-MPVPE, and AUC as the number of optimization iterations increases. Right: Relative PA-MPVPE improvement under different numbers of visible keypoint conditions as the optimization iteration increases.